

1 **Validation of Ocean Model Predictions of Mean**
2 **Dynamic Topography in Shallow, Tidally Dominated**
3 **Regions Using Observations of Overtides**

4 **C. Renkl¹ and K. R. Thompson¹**

5 ¹Department of Oceanography, Dalhousie University, Halifax NS, Canada

6 **Key Points:**

- 7 • Observed overtides are useful in specifying ocean model bathymetry in tidally dom-
8 inated regions.
- 9 • They can also be used to validate, and physically interpret, mean dynamic topog-
10 raphy predicted by ocean models.
- 11 • Overtides are useful in the design of geodetic and ocean observing systems in tidally
12 dominated regions.

Abstract

In shallow, tidally dominated regions, overtides and the mean state of the ocean are coupled through their simultaneous generation by nonlinear processes. We present a new method that uses observed overtides (e.g., M_4) and mean currents to independently assess the accuracy of mean dynamic topography (MDT) predicted by ocean models. This is useful in regions where no sufficiently long, geodetically referenced sea level records are available for validation of the predicted MDT.

We apply the new method to a regional model of the Gulf of Maine/Scotian Shelf region (GoMSS) and a barotropic, higher resolution model focused on the upper Bay of Fundy (UBoF). We first show that the tides and mean circulation predicted by UBoF are in good agreement with observations and a significant improvement over GoMSS. Next, we use UBoF to demonstrate that observed overtides are useful in specifying the bathymetry and parameters of an ocean model. An accurate bathymetry is critical for capturing the dominant nonlinear processes that generate overtides and control the form of MDT in shallow, tidally dominated regions. Finally, we use the observed overtides to argue that the MDT predicted by UBoF is more realistic than the prediction by GoMSS. In the vicinity of headlands, both horizontal advection and bottom friction in UBoF generate harmonics of the tidal flow and local setdowns of coastal MDT of $\mathcal{O}(10\text{ cm})$. The prediction of such features, validated by observed overtides, can provide guidance in future deployments of tide gauges in support of geoid and ocean model validation.

Plain Language Summary

Overtides are higher harmonics of the main astronomical tidal constituents. They are often observed in shallow, tidally dominated regions and are dynamically linked to spatial variations in the mean state. In this study, we use observed overtides to compare predictions by a regional model of the Gulf of Maine/Scotian Shelf region (GoMSS) and a simpler, but higher resolution, model of the upper Bay of Fundy (UBoF). It is first shown that the tides and mean circulation predicted by UBoF are in good agreement with observations and a significant improvement over GoMSS. UBoF is then used to demonstrate that observed overtides are useful in optimizing the configuration of ocean models, including the representation of the sea floor. We next show that observed overtides can be used to assess the accuracy of the mean state predicted by ocean models, including spatial variations in mean sea level. An advantage of this approach is that overtides can

45 be estimated from short records of sea level and currents thereby increasing the num-
46 ber of locations at which models can be assessed. Finally, we argue that ocean models
47 validated using overtides can provide guidance in the design of geodetic an ocean observ-
48 ing systems in tidally dominated regions.

49 1 Introduction

50 Mean dynamic topography (MDT) is the height of the mean sea level above the
51 geoid after removal of the inverse barometer effect (e.g., Hughes & Bingham, 2006). The
52 MDT includes contributions from spatial changes in sea water density, mean setup due
53 to local winds and nonlinear processes such as the Bernoulli setdown due to tidal cur-
54 rents around headlands. In the open ocean, mean surface currents are approximately in
55 geostrophic balance leading to a simple relationship between MDT and mean surface cir-
56 culation. As the coast is approached the interpretation of alongshore changes in MDT
57 becomes more subtle because the geostrophic balance is not longer dominant in the along-
58 shore direction and frictional processes become more important (e.g., Lentz & Fewings,
59 2012; Higginson et al., 2015; Hughes et al., 2019).

60 Despite the subtlety of the alongshore momentum balance, it is still useful for prac-
61 tical applications. A particularly simple illustration is provided by considering a constant
62 density ocean in a rectangular basin of constant depth lying on a mid-latitude β -plane.
63 If the ocean circulation is forced by a steady, purely zonal wind stress varying with lat-
64 itude, the meridional Sverdrup flow integrated across the basin is balanced by a return
65 flow in a narrow western boundary current (e.g., Stommel, 1948; Munk, 1950). It is straight-
66 forward to show, using simple vorticity arguments, that the tilt of MDT along the west-
67 ern coastal boundary is proportional to the meridional transport of the boundary cur-
68 rent and independent of the details of the frictional dissipation in the model (e.g., Thomp-
69 son et al., 1986). Stewart (1989) showed that this extends to inertial western boundary
70 layers.

71 Estimates of MDT along the coast, with standard errors typically less than 3 cm,
72 can now be made using long tide gauge records and the latest generation of geoid mod-
73 els (henceforth the geodetic approach, Woodworth et al., 2012; Huang, 2017). These new
74 estimates have proved useful in validating predictions of alongshore variations of MDT
75 by ocean models (henceforth the hydrodynamic approach) and also their predictions of

76 mean circulation on both basin and global scales (e.g., Woodworth et al., 2012; Higgin-
77 son et al., 2015; Lin et al., 2015). Agreement between MDT predicted by the geodetic
78 and hydrodynamic approaches increases confidence in both the geoid and ocean mod-
79 els.

80 The geodetic approach to estimating coastal MDT is limited to locations where decades
81 of sea level observations, made by tide gauges with continuous vertical datum control,
82 exist. This limits severely the number of locations at which the geodetic approach can
83 be used. Here, we propose a fundamentally different approach to evaluate model pre-
84 dictions of coastal MDT using observations of overtides (higher harmonics of the main
85 astronomical tidal constituents; e.g., Le Provost, 1991). This approach has two impor-
86 tant advantages: it does not require information about the geoid and it can be applied
87 to relatively short, $\mathcal{O}(1 \text{ month})$, sea level records, thereby greatly increasing the num-
88 ber of locations at which the ocean models can be validated.

89 Overtides are generated by nonlinear processes involving sea level and currents, e.g.,
90 horizontal advection and dissipation by bottom friction. They have been studied exten-
91 sively using analytical and numerical models as well as observations (e.g., Pingree & Mad-
92 dock, 1978; Aubrey & Speer, 1985; Speer & Aubrey, 1985; Friedrichs & Aubrey, 1988;
93 Parker, 1991; Le Provost, 1991). Comparing observed and predicted overtides provides
94 information about the ability of ocean models to capture these dominant nonlinear pro-
95 cesses (Pingree & Maddock, 1978). It has been shown that the same nonlinear processes
96 can have a direct influence on mean sea level (e.g., Pingree et al., 1984; Li & O'Donnell,
97 1997, 2005). This raises the possibility of validating the mean state of an ocean model
98 by assessing the accuracy of its predicted overtides.

99 The initial motivation for the present study was the need to assess the realism of
100 a large ($\sim 10 \text{ cm}$) setdown of MDT in the upper reaches of the Bay of Fundy predicted
101 by the Gulf of Maine and Scotian Shelf model (GoMSS, Katavouta & Thompson, 2016).
102 Based on theoretical considerations, we expected a small setup of a few centimeters. Un-
103 fortunately no long, geodetically referenced, tide gauge records were available for the study
104 region. This encouraged us to explore the use of overtides in the validation of the pre-
105 dicted setdown.

106 The Bay of Fundy, together with the Gulf of Maine, is a near-resonant system with
107 an extreme tidal range at the M_2 tidal frequency (Garrett, 1972). The present study will

108 focus on Minas Channel, Minas Basin and Cobequid Bay (Figure 1) where the highest
109 tides in the world have been observed. In such shallow, tidally dominated regions, the
110 largest overtide is expected to be the first harmonic M_4 (Speer et al., 1991). For refer-
111 ence, the periods of M_2 and M_4 are 12.42 h and 6.21 h, respectively.

112 The tidal dynamics and mean circulation of the Bay of Fundy have been the sub-
113 ject of numerous modelling and observation programs (e.g., Tee, 1977; Greenberg, 1983;
114 Dupont et al., 2005; Karsten et al., 2008; Hasegawa et al., 2011; Wu et al., 2011). Many
115 of these earlier studies were motivated by the need for reliable assessments of the impact
116 of tidal energy extraction, including the effect on near and far field sediment transport.
117 However, the MDT of the region has not been discussed.

118 The approach described in this study has wider applicability than just checking the
119 accuracy of the MDT predicted by GoMSS in the Bay of Fundy. From an oceanogra-
120 pher’s perspective, this study justifies the use of overtides in the validation of the mean
121 state predicted by ocean models in tidally dominated regions. From a geodesist’s per-
122 spective, an ocean model that has been validated using observed overtides is a poten-
123 tially more reliable tool for assessing geoid models in tidally dominated regions. The same
124 ocean model can also be used with more confidence to select the location of tide gauges
125 for future long-term measurements of sea level in support of geoid model validation, and
126 also correcting existing mean sea levels for localized oceanographic effects.

127 Based on the above discussion, the following three questions will be addressed with
128 particular emphasis on the upper Bay of Fundy. In tidally dominated regions, are ob-
129 served overtides useful in (i) specifying the bathymetry and parameters of ocean mod-
130 els (ii) validating predicted MDT, and (iii) the design of geodetic and ocean observing
131 systems.

132 The structure of this study is as follows. Section 2 provides a brief overview of the
133 generation of overtides and their relationship to MDT with particular attention paid to
134 tidal flow through channels and past headlands. Both of these flow regimes play an im-
135 portant role in shaping the MDT in the Bay of Fundy. In Section 3, the GoMSS model
136 is described and a high-resolution model for the upper Bay of Fundy is introduced. Sec-
137 tion 4 describes the observations used in Section 5 to validate the ocean models. The pre-
138 dicted MDT is described in Section 6 along with its sensitivity to horizontal resolution,

139 lateral viscosity and bottom friction parameters. The results are summarized and dis-
 140 cussed in Section 7.

141 2 Background and Theory

142 This section provides the theoretical background required to justify the use of over-
 143 tides in the evaluation of ocean model predictions of the mean state with a particular
 144 focus on MDT. Following a general discussion of the generation of overtides, two situ-
 145 ations of particular relevance to the present study are discussed: tidal flow around a head-
 146 land and along a narrow channel closed at one end.

147 The underlying momentum and continuity equations are taken to be (Robinson,
 148 1983):

$$149 \frac{\partial \mathbf{u}}{\partial t} + \mathbf{u} \cdot \nabla \mathbf{u} + f \hat{\mathbf{k}} \times \mathbf{u} = -g \nabla \eta - c_d \frac{\mathbf{u} |\mathbf{u}|}{h} + A_h^m \nabla^2 \mathbf{u}, \quad (1)$$

$$150 \frac{\partial \eta}{\partial t} + \nabla \cdot (h \mathbf{u}) = 0. \quad (2)$$

152 Here, $\mathbf{u}(\mathbf{x}, t) = u \hat{\mathbf{i}} + v \hat{\mathbf{j}}$ is the horizontal current averaged over the total water depth

$$153 h = H + \eta, \quad (3)$$

154 where H is the water depth at rest and η is the height of the sea surface above the geoid.
 155 The horizontal unit vectors $\hat{\mathbf{i}}$ and $\hat{\mathbf{j}}$ in zonal and meridional direction, respectively, are
 156 perpendicular to the orientation of local gravity indicated by the unit vector $\hat{\mathbf{k}}$. f is the
 157 Coriolis parameter and g is the vertical acceleration due to gravity. A quadratic bottom
 158 friction law is assumed with constant drag coefficient c_d . A_h^m is the horizontal eddy vis-
 159 cosity coefficient. Atmospheric forcing and density variations have been ignored along
 160 with terms that arise from the vertical shear of the current on depth-averaging the hor-
 161 izontal advection term (Robinson, 1983).

162 The momentum equation (1) has two nonlinear terms related to horizontal advec-
 163 tion and bottom friction. The continuity equation (2) has a single nonlinear term involv-
 164 ing the product of η and \mathbf{u} . If the system is forced by a single tidal constituent, all three
 165 terms can individually generate both overtides and a change in the mean state (e.g., Parker,
 166 1991). As will be discussed below, the relationship between overtides and the mean state
 167 is not straightforward and depends on the nonlinearities that generate them (e.g., Pin-
 168 gree et al., 1984).

169 The vorticity equation can provide physical insights into the generation of overtides.
 170 The curl of (1) leads to the following equation governing evolution of relative vorticity ζ
 171 (e.g., Signell & Geyer, 1991):

$$172 \quad \frac{\partial}{\partial t} (f + \zeta) + \mathbf{u} \cdot \nabla (f + \zeta) = \frac{(f + \zeta)}{h} \mathbf{u} \cdot \nabla h - \hat{\mathbf{k}} \cdot \nabla \times \left(c_d \frac{\mathbf{u} |\mathbf{u}|}{h} \right) + A_b^m \nabla^2 \zeta. \quad (4)$$

173 The terms on the right-hand side of (4) correspond to changes in ζ due to vortex tube
 174 stretching, and torques involving bottom stress and lateral friction. The bottom friction
 175 term can be decomposed in a dissipation term and two generation terms associated with
 176 spatial changes in water depth and current speed (Signell & Geyer, 1991). The vortic-
 177 ity equation will prove useful in the following discussion of flow around headlands, and
 178 also the interpretation of MDT.

179 **2.1 Tidal Flow Around a Headland**

180 In a seminal study of tides in the Bay of Fundy, Tee (1976) used a numerical model
 181 based on (1) and (2) to show how the combined effect of vorticity generation and its sub-
 182 sequent advection could generate strong mean flows in the vicinity of headlands with speeds
 183 approaching 1 m s^{-1} . The predictions by the model were subsequently shown to agree
 184 well with current measurements (Tee, 1977). Similar results have been found for other
 185 locations and it is now generally accepted that strong tidal flow past a headland can lead
 186 to flow separation and two permanent, counter-rotating eddies on each side of the head-
 187 land that drive a mean flow along the coast toward the tip (e.g., Pingree & Maddock,
 188 1977; Robinson, 1983; Geyer & Signell, 1990). It has also been shown that tidal flow past
 189 a headland can generate overtides in addition to a mean flow (Mardell & Pingree, 1981;
 190 Geyer & Signell, 1990).

191 Signell and Geyer (1991, hereafter SG91) used a combination of analytical and nu-
 192 merical models based on (1) and (2) to examine the formation and evolution of transient
 193 eddies generated by tidal flow past an idealized headland. As a first step, SG91 used an
 194 analytical model to determine the conditions under which the flow separates from the
 195 coast (see their Section 3.2). In this model, they assumed an elliptically shaped head-
 196 land protruding from the x -axis and a thin shoaling region around it where the water
 197 depth decreases linearly toward the coast. Using boundary layer techniques, they argued
 198 that, in the absence of flow separation, the pressure gradient along the coast can be ap-

199 proximated by

$$200 \quad g \frac{\partial \eta}{\partial s} = - \frac{\partial u_1}{\partial t} - u_1 \frac{\partial u_1}{\partial s} - c_d \frac{U_0 u_1}{H}, \quad (5)$$

201 where s is the alongshore coordinate and $u_1(s, t)$ is the tidal current along the coast. To
 202 specify u_1 they assumed a large-scale irrotational flow, varying in time with tidal frequency ω
 203 as $\sin(\omega t)$. SG91 gave an analytic expression for $u_1(s, t)$ that satisfies the coastal bound-
 204 ary condition of no normal flow and approaches $U_0 \sin(\omega t)$ with increasing distance from
 205 the headland. Substituting the expression for $u_1(s, t)$ into (5) resulted in an analytic ex-
 206 pression for the time varying pressure gradient along the coast of the headland. SG91
 207 used this pressure gradient to determine the location, and stage of the tide, at which the
 208 pressure gradient was adverse (i.e., increasing pressure in the downstream direction) lead-
 209 ing to possible flow separation.

210 Equation (5) has one nonlinearity related to advection that leads to a Bernoulli set-
 211 down of sea level, $u_1^2/2g$. The tidal current u_1 is a separable function of location and time,
 212 so we can write $u_1(s, t) = U_1(s) \sin(\omega t)$. As a result, the Bernoulli setdown can be ex-
 213 pressed as a local change in mean sea level and an overtide of sea level varying at twice
 214 the frequency of the tidal forcing:

$$215 \quad \frac{u_1^2}{2g} = \frac{U_1^2}{2g} - \frac{U_1^2}{2g} \cos(2\omega t). \quad (6)$$

216 It follows that if one were to determine the overtide in sea level, it would be possible to
 217 also determine the mean Bernoulli setdown. A typical tidal current near a headland in
 218 the Bay of Fundy is $U_1 = 1.5 \text{ m s}^{-1}$. This results in both an M_4 amplitude in sea level,
 219 and a mean Bernoulli setdown of about 10 cm. Bernoulli setdown provides a particularly
 220 simple demonstration of how knowledge of overtides can provide information about MDT.

221 As the strength of the large-scale tidal flow (U_0) increases (see SG91 for conditions),
 222 the momentum balance (5) eventually breaks down due to flow separation. SG91 used
 223 a numerical model, based on a discretization of (1) and (2), to examine the generation
 224 and movement of the transient eddies generated by the oscillating flow past the head-
 225 land. They showed that relative vorticity is primarily generated by bottom friction in
 226 the shoaling region around the headland and subsequently transported into the interior
 227 where it dissipates over a tidal cycle. After the tide reverses, the same mechanism in-
 228 jects relative vorticity of opposite sign on the other side of the headland. As a consequence,
 229 the mean circulation is characterized by a pair of counter-rotating eddies on either side

230 of the promontory consistent with the results of Tee (1976). These eddies drive a mean
 231 flow along both sides of the headland toward the tip.

232 The mean Bernoulli setdown in the numerical model of SG91 is greatest at the tip
 233 of the headland where the tidal current is strongest. In order to drive the mean coastal
 234 flow toward the tip of the headland, an additional setdown of sea level is needed to pro-
 235 vide an alongshore pressure gradient to overcome friction. (The coastal boundary con-
 236 dition of no normal flow eliminates the Coriolis term.) More quantitatively, the mean
 237 sea level gradient required to overcome the friction opposing the time mean current \bar{u}
 238 can be approximated by $\lambda\bar{u}/gH_0$ where $\lambda = 8c_d U_1/3\pi$ is a linear drag coefficient (e.g.,
 239 Proudman, 1953), and H_0 is the water depth near the coast. Taking typical values for
 240 the Bay of Fundy of $c_d = 2.5 \times 10^{-3}$, $\bar{u} = 0.3 \text{ m s}^{-1}$, and $H_0 = 10 \text{ m}$ gives a gradient
 241 in mean sea level along the coast of 10 cm over 10 km. This is on the same order as the
 242 Bernoulli setdown. We will see exactly this type of feature in the predicted MDT for the
 243 upper Bay of Fundy.

244 **2.2 Tidal Flow Along a Narrow Channel**

245 It is well known (e.g., Pingree et al., 1984; Parker, 1991; Li & O'Donnell, 1997, 2005)
 246 that the nonlinear terms in (1) can generate a mean circulation in a narrow channel closed
 247 at one end. Li and O'Donnell (2005) used a perturbation technique to analyze the ef-
 248 fect of channel length on the mean circulation in tidally dominated channels with lat-
 249 eral depth variations. They showed that mean sea level over a tidal cycle always increases
 250 toward the head of the channel when forced at the mouth by a tide with a single frequency.
 251 They explained this setup in terms of the superposition of an incident and reflected wave
 252 that are both attenuated by bottom friction. Because the travel path of the reflected wave
 253 is longer, it is more strongly attenuated than the incident wave leading to the mean setup
 254 of sea level. The magnitude of the setup depends on the ratio of the channel length and
 255 the wavelength of the tidal forcing. For a channel of 5–150 km length with depth vary-
 256 ing laterally between 5 and 10 m, the setup can reach up to 12 cm given semi-diurnal forc-
 257 ing.

258 The quadratic bottom friction term in (1) can also generate variability locally at
 259 the frequencies of even and odd harmonics of the incoming tidal wave (e.g., Parker, 1991).
 260 This tidal flow along a narrow channel is another example of the link between the mean

261 state and overtides and will be important in explaining the distribution of predicted MDT
 262 near the head of the upper Bay of Fundy.

263 3 Ocean Models

264 Two models are used in this study. The three-dimensional, fully nonlinear, baro-
 265 clinic ocean model of the Gulf of Maine and Scotian Shelf (GoMSS) was developed by
 266 Katavouta and Thompson (2016). A higher resolution barotropic model of the upper Bay
 267 of Fundy, within the model grid of GoMSS, was developed specifically for this study. This
 268 new model will henceforth be referred to as UBoF. The domains of both models are shown
 269 in Figure 1. Further details are given below.

270 3.1 GoMSS

271 For the present study, the GoMSS model was upgraded to version 3.6 of the Nu-
 272 cleus for European Modelling of the Ocean (NEMO, Madec et al., 2017). The x -axis of
 273 the coordinate system is aligned with the large-scale orientation of the coastline with an
 274 anti-clockwise rotation of 23.6° relative to geographic coordinates (E-W, S-N). The hor-
 275 izontal grid spacing is $1/36^\circ$ which corresponds to 2.1–2.5 km in the x -direction and 2.9–
 276 3.6 km in the y -direction.

277 In the vertical, the model grid consists of 52 levels which, in a state of rest, increase
 278 in spacing from 0.72 m at the surface to 235.33 m at the bottom. The maximum depth
 279 of the bathymetry is clipped at 4000 m. GoMSS uses the z^* -coordinate approach (Levier
 280 et al., 2007) which allows for large variations of the (nonlinear) free surface. In this vari-
 281 able volume formulation the level spacing varies over time with sea surface height. At
 282 the bottom, partial cells are used to better resolve the bathymetry.

283 The TKE turbulent closure scheme used in the original configuration of GoMSS
 284 was replaced by the k - ϵ -closure scheme (Rodi, 1987) using the Generic Length Scale (GLS)
 285 formulation (Umlauf & Burchard, 2003, 2005). The enhanced vertical diffusion of mo-
 286 mentum applied in the original configuration was turned off. Furthermore, an iso-level
 287 Laplacian diffusion operator is used instead of a biharmonic operator for stability rea-
 288 sons. The background lateral eddy viscosity coefficient A_h^m was taken to be $50 \text{ m}^2 \text{ s}^{-1}$ (Ta-
 289 ble 1).

290 A nonlinear parameterization of bottom friction, with enhancement in the logarithmic
 291 boundary layer, is used. This means the drag coefficient c_d is dependent on the thick-
 292 ness of the model grid cell above the bottom. The minimum value of c_d was set to 2.5×10^{-3} (Ta-
 293 ble 1). At the coast, a partial slip boundary condition with a slip parameter of 0.5 is ap-
 294 plied (see Madec et al., 2017, for details).

295 GoMSS was initialized on 1 January 2010 and run for three months. For the ini-
 296 tial and lateral boundary conditions, temperature, salinity, sea surface height and cur-
 297 rents were taken from the HYCOM-NCODA system (Chassignet et al., 2007). The bound-
 298 ary forcing was supplemented with tidal elevations and currents computed using five con-
 299 stituents (M_2 , N_2 , S_2 , K_1 , O_1) from FES2004 (Lyard et al., 2006). Surface forcing at the
 300 air-sea interface was taken from the Climate Forecast System Reanalysis (Saha et al.,
 301 2010).

302 Given GoMSS is initialized with realistic, three-dimensional hydrographic informa-
 303 tion, the spin-up of the model depends primarily on the tides. Based on sensitivity stud-
 304 ies, the spin-up time is estimated to be 2 days. The tidal amplitudes and phases presented
 305 below are estimated from the last month of the three month simulation.

306 3.2 UBoF

307 The strong tidal flow in the Bay of Fundy mixes the water column and therefore
 308 vertical stratification is negligible (Tee, 1977). For this reason, UBoF is a barotropic model
 309 with constant temperature and salinity forced only by tides along its open boundary. UBoF
 310 is based on the same version of NEMO as GoMSS, but only covers the upper Bay of Fundy
 311 (Figure 1b). In comparison to GoMSS, the UBoF horizontal grid is refined by a ratio
 312 of 4 resulting in an average grid spacing of 555 m in the along domain direction (roughly
 313 to the NE) and 785 m in the cross-domain direction. The vertical grid, turbulence clo-
 314 sure schemes, and the formulation of the lateral diffusion operator, are the same as in
 315 GoMSS. Although the model grid is three-dimensional, the underlying dynamics are well
 316 represented by the depth-averaged equations (1) and (2).

317 The bathymetry for UBoF was created by combining the 30'' General Bathymet-
 318 ric Chart of the Oceans (GEBCO, Weatherall et al., 2015) with more than 122 000 high-
 319 resolution in-situ measurements using optimal interpolation. Note that NEMO version
 320 3.6 does not allow for wetting and drying of model grid cells and therefore, a minimum

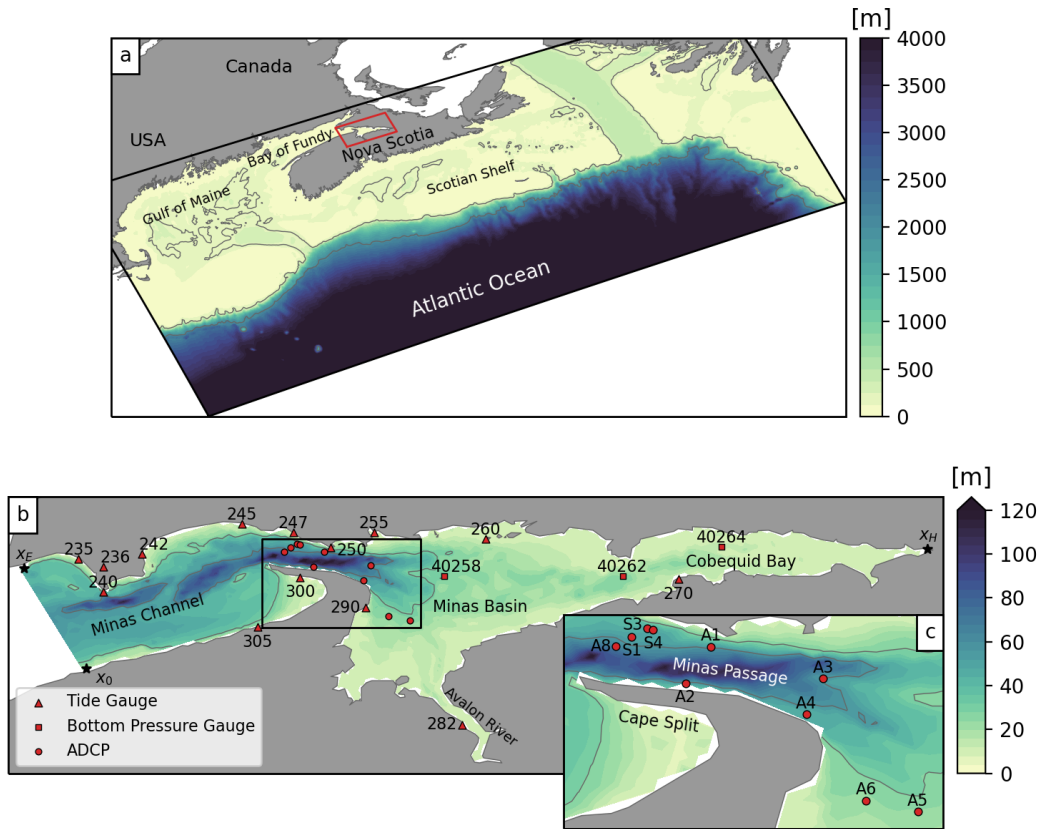


Figure 1. Model domains and observation locations. (a) Model domain and bathymetry of the GoMSS model; contours indicate the 200 and 2000 m isobaths. The red rectangle defines the model domain of UBoF which is shown in detail in panel (b) where contours mark the 30 and 60 m isobaths. Triangles and squares show the positions of the tide gauges and bottom pressure gauges, respectively, used in this study. Circles mark the locations of ADCP measurements. Black stars are alongshore reference points used throughout this study. (c) Enlarged view of the UBoF model domain in the vicinity of Cape Split (see black rectangle in panel b).

321 water depth has to be specified. We use the approach of Maraldi et al. (2013) to take
 322 into account the spatially varying maximum tidal amplitude.

323 The prediction of tides by non-global ocean models is strongly dependent on the
 324 quality of the open boundary conditions. UBoF was forced with tidal elevation and cur-
 325 rents for five semi-diurnal and diurnal constituents (M_2 , S_2 , N_2 , K_1 , O_1) obtained from
 326 the Scotia-Fundy-Maine Data of WebTide (Dupont et al., 2005). WebTide is a tidal pre-
 327 diction model that assimilates tidal amplitudes and phases estimated from satellite al-
 328 timetry data at crossover points. Predictions by WebTide have been shown to be in ex-
 329 cellent agreement with observations throughout the Bay of Fundy system (see follow-
 330 ing section for details).

331 The control run of UBoF (henceforth CTRL, Table 1) was chosen based on the val-
 332 idation of multiple runs. Runs B1–B3 use the same high-resolution grid and model pa-
 333 rameters as CTRL, but the bathymetry has been replaced by the GoMSS bathymetry
 334 interpolated to the UBoF grid using three different interpolation schemes. The “S” runs
 335 explore the effect of varying the background lateral eddy viscosity coefficient A_n^m and min-
 336 imum bottom friction coefficient c_d . (“S” stands for sensitivity.)

337 The amplitude and phase of the predicted tidal elevation of the models were com-
 338 puted using the harmonic analysis in NEMO. Ellipse parameters of the tidal currents
 339 were estimated from the hourly predictions of depth-averaged currents using a simple
 340 (no inference) least squares method. A Rayleigh criterion of 0.95 was used in the selec-
 341 tion of fitted constituents. Prior to tidal analysis, the predicted horizontal current com-
 342 ponents, which are defined on the Arakawa C-grid of the model, were linearly interpo-
 343 lated to the center of each grid cell. The current vectors were then rotated from the grid
 344 coordinates to geographic coordinates. Predicted tidal ellipse parameters and mean cur-
 345 rents were then estimated from the time series at the center model grid points closest
 346 to the ADCP locations in Figure 1.

347 4 Observations

348 Tidal amplitudes and phases, estimated from sea level records from 14 coastal tide
 349 gauges, were provided by the Canadian Hydrographic Service (CHS, S. Nudds, 2017, per-
 350 sonal communication). Additional observations made by three bottom pressure gauges

Table 1. Overview of model runs. GoMSS (1/36° grid spacing) is the Gulf of Maine and Scotian Shelf regional ocean model. CTRL is the control run of the barotropic high-resolution ocean model UBoF (1/144° grid spacing) covering the upper Bay of Fundy (see Figure 1). Runs B1–B3 use the same high-resolution grid and model parameters as CTRL, but the bathymetry is replaced by the GoMSS bathymetry estimated using three interpolation schemes. The “S” runs explore the effect of varying the background lateral eddy viscosity coefficient A_h^m and minimum bottom friction coefficient c_d (see text). All model runs are for three months starting 1 January, 2010.

Run	Model	Bathymetry	A_h^m [m ² /s]	c_d [$\times 10^{-3}$]
GoMSS	GoMSS	ETOPO2v2*	50	2.5
CTRL	UBoF	GEBCO & Observations	20	4.0
B1	UBoF	GoMSS, nearest neighbor	20	4.0
B2	UBoF	GoMSS, linear interpolation	20	4.0
B3	UBoF	GoMSS, cubic interpolation	20	4.0
S	UBoF	GEBCO & Observations	10, 20, ..., 50	2.5, 3.0, ..., 4.5

* Higher-resolution data were used to improve the bathymetry in the inner Gulf of Maine (see Katavouta & Thompson, 2016, for details).

351 were made available by Dr. D. Greenberg (Bedford Institute of Oceanography, BIO, 2018,
352 personal communication). Figure 1b shows the locations of all 17 observation sites.

353 The number of constituents resolved by the tidal analyses depends on record length.
354 This ranges from 21 to 197 days across the 17 locations. It was possible to resolve M_2 ,
355 S_2 , N_2 , K_1 , O_1 and M_4 at all sites, except for N_2 at Spencer Island (station 242). The
356 longest available sea level record (168 days) was for Cape D'Or. (station 240). It was
357 obtained from the Marine Environmental Data Section (MEDS) of the Department of
358 Fisheries and Oceans Canada. To quantify the uncertainty of the amplitudes and phases
359 estimated from the shorter records, the 168-day record from Cape D'Or was split into
360 non-overlapping 29-day blocks and a tidal analysis was performed on each block. The
361 standard deviation of the estimated amplitudes and phases was then used to obtain ap-
362 proximate 95% confidence intervals for 29-day records. The halfwidth of the confidence
363 intervals was found to be 0.09 m for the semi-diurnal amplitudes and 1° , 5° and 7° for
364 the phases of M_2 , N_2 and S_2 , respectively. These values are similar to the estimates made
365 by Dupont et al. (2005) based on an analysis of an 89-day observed record from Minas
366 Basin. For the diurnal and M_4 tides, the halfwidths of the 95% confidence intervals are
367 at the millimeter level for the amplitudes and 1° , 2° and 2° for the phases of K_1 , O_1 and
368 M_4 , respectively.

369 Observed tidal ellipse parameters and the time mean of depth-averaged current,
370 both obtained from Wu et al. (2011), are also used to validate the model predictions. These
371 estimates are based on observations made by bottom-mounted Acoustic Doppler Cur-
372 rent Profilers (ADCPs) deployed at ten stations in Minas Passage and Minas Basin (Fig-
373 ure 1c for locations). The lengths of the ADCP records range between 21 and 41 days.
374 For additional details of the ADCP observations, and the data processing, see Wu et al.
375 (2011).

376 5 Validation of Tides and Mean Current

377 We first validate the control run of UBoF (CTRL, Table 1) for M_2 elevation and
378 currents. Next, we validate M_4 elevation and currents, and finally the mean currents.
379 This is the first time that a tidal model of the upper Bay of Fundy has been validated
380 using observed values of M_4 tidal elevation. The MDT, for which no reliable observa-
381 tions exist, is discussed in the following section.

In addition to root mean squared error (RMSE), the following metric is used to validate the predicted tides at N stations:

$$\tilde{\gamma}^2 = \frac{\sum_{i=1}^N \int_0^T |\tilde{\mathbf{x}}_{o,i}(t) - \tilde{\mathbf{x}}_{m,i}(t)|^2 dt}{\sum_{i=1}^N \int_0^T |\tilde{\mathbf{x}}_{o,i}(t)|^2 dt}. \quad (7)$$

Here, $\tilde{\mathbf{x}}_{o,i}$ and $\tilde{\mathbf{x}}_{m,i}$ are the observed and predicted tidal variables, respectively, for station i . Each variable is expressed as a sinusoidal function of time t with frequency $\omega = 2\pi/T$, where T is the tidal period. The $\tilde{\gamma}^2$ metric can be used to assess the fit of either tidal elevations or currents. For the latter it takes into account errors in the principal axes of tidal current and also phase. This metric is based on Katavouta et al. (2016) but has been extended to summarize the fit for multiple stations.

The mean currents are validated in a similar way:

$$\bar{\gamma}^2 = \frac{\sum_{i=1}^N |\bar{\mathbf{u}}_{o,i} - \bar{\mathbf{u}}_{m,i}|^2}{\sum_{i=1}^N |\bar{\mathbf{u}}_{o,i}|^2}, \quad (8)$$

where $\bar{\mathbf{u}}_{o,i}$ and $\bar{\mathbf{u}}_{m,i}$ are the observed and predicted mean currents at observation location i . The bar indicates a time mean.

For both metrics, the smaller γ^2 the better the fit of the model to the observations: $\gamma^2 = 0$ implies a perfect model fit. If $\gamma^2 > 1$, the model has no useful skill. Both metrics can be used to assess fit at one or more ($N > 1$) stations.

5.1 M₂ Elevations and Currents

The amplitude and phase of the M₂ tidal elevations predicted by CTRL are shown in Figure 2. Panel (a) shows the predicted amplitude and phase across the whole model domain and panels (b) and (c) show the amplitude and phase along the coast. The x -axis in these two panels is alongshore distance measured counterclockwise from x_0 on the open boundary, to the head at x_H , and then along the north shore to x_E where the coastline intersects the open boundary. The black circles in all three panels show the locations of coastal tides gauges along the south shore. The black triangles are for locations along the north shore.

Along the open boundary (clockwise from x_0 to x_E), the predicted mean M₂ amplitude is 4.07 m and it increases to 5.96 m at the head of Cobequid Bay (x_H). The tidal phase also increases toward the head with high water arriving at x_H with a delay of about 1.5 h relative to the open boundary. The predicted increase in M₂ amplitude and phase toward the head is consistent with previous studies (e.g., Greenberg, 1969; Tee, 1976;

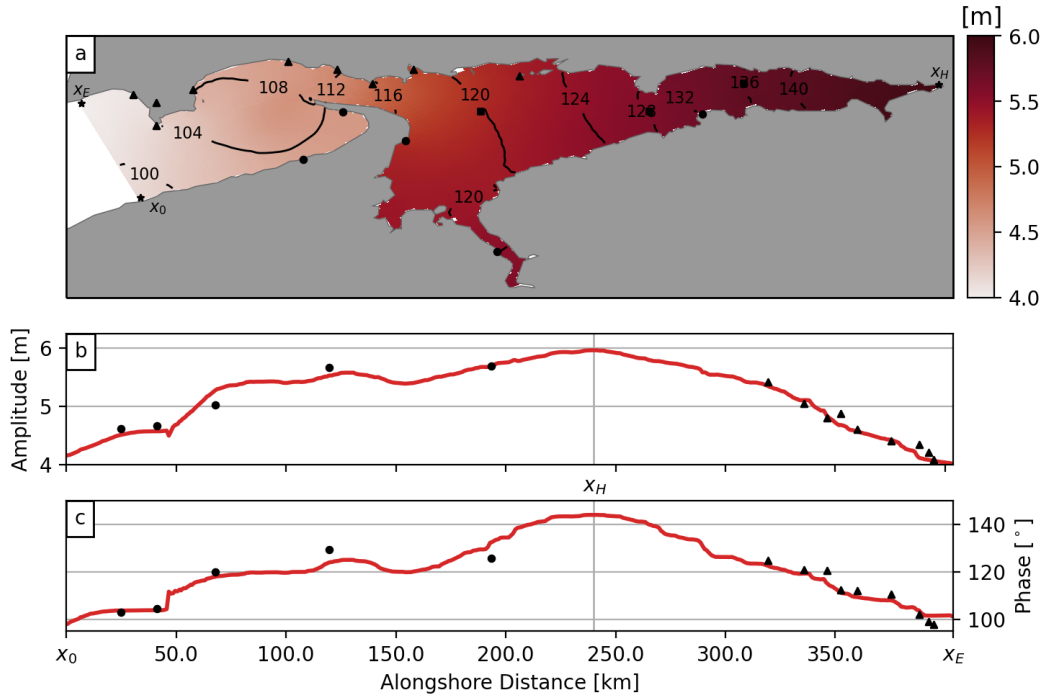


Figure 2. Predicted and observed amplitude and phase of M_2 tidal elevation. (a) Colors show the tidal amplitude in meters and contours show phase in degrees relative to Greenwich predicted by CTRL. Circles and triangles mark the tide gauges along the southern and northern coast, respectively. Squares indicate offshore locations. Black stars mark alongshore reference points. Panels (b) and (c) show M_2 tidal amplitude and phase as a function of alongshore distance from x_0 . Black markers indicate observed values at the coastal tide gauges shown in panel (a).

Table 2. Summary of fit of model predictions to sea level and current observations using the γ^2 metric. Predicted sea level (η) and depth mean current (\mathbf{u}) have been validated against observations at several tidal frequencies and the mean. The UBoF runs (CTRL and “S” runs) are defined in Table 1. The same metrics are given for GoMSS and WebTide (last two columns). The same observations from 14 coastal tide gauges, 3 bottom pressure gauges and 10 ADCPs were used for all models. The γ^2 metrics are defined by (7) and (8).

Variable	Constituent	CTRL	“S” runs	GoMSS	WebTide
η	M ₂	0.005	0.005–0.007	0.018	0.006
η	S ₂	0.022	0.021–0.024	0.325	0.022
η	N ₂	0.050	0.047–0.055	0.079	0.042
η	M ₄	5.577	5.089–6.072	16.887	1.841
\mathbf{u}	M ₂	0.023	0.022–0.027	0.201	0.034
\mathbf{u}	M ₄	0.329	0.325–0.393	1.924	0.325
\mathbf{u}	Mean	0.303	0.264–0.410	0.876	-

412 Karsten et al., 2008; Hasegawa et al., 2011; Wu et al., 2011) and has been explained in
 413 terms of the resonant character of the Bay of Fundy system (Garrett, 1972).

414 The agreement between the observed and predicted M₂ elevation at the 14 coastal
 415 tide gauges is shown by the black dots and triangles along the south shore and north shore,
 416 respectively, in Figures 2b and c. The RMSEs in amplitude and phase are 0.12 m and
 417 3.4°, respectively, and $\tilde{\gamma}^2 = 0.005$. Using observations from all 14 coastal tide gauges,
 418 and the three additional pressure gauges shown by the black squares in Figure 2a, the
 419 RMSEs are 0.17 m and 3.5° for amplitude and phase, respectively, and $\tilde{\gamma}^2 = 0.005$. These
 420 error metrics are similar to those of WebTide based on the same observations (RMSEs
 421 for amplitude and phase are 0.13 m and 4.03°, respectively; $\tilde{\gamma}^2 = 0.006$, see Table 2).
 422 This is not surprising because UBoF is forced with tidal elevations taken from WebTide
 423 (see Section 3).

424 Next, the fit of the model to the observed, depth-mean M₂ tidal currents at the ten
 425 ADCP locations is examined (Figure 1c). The M₂ tidal ellipses are shown in Figure 3.
 426 The dots correspond to the position of the tidal current at the time of the maximum equi-
 427 librium tide at the Greenwich meridian. Strong, rectilinear M₂ tidal currents are evident

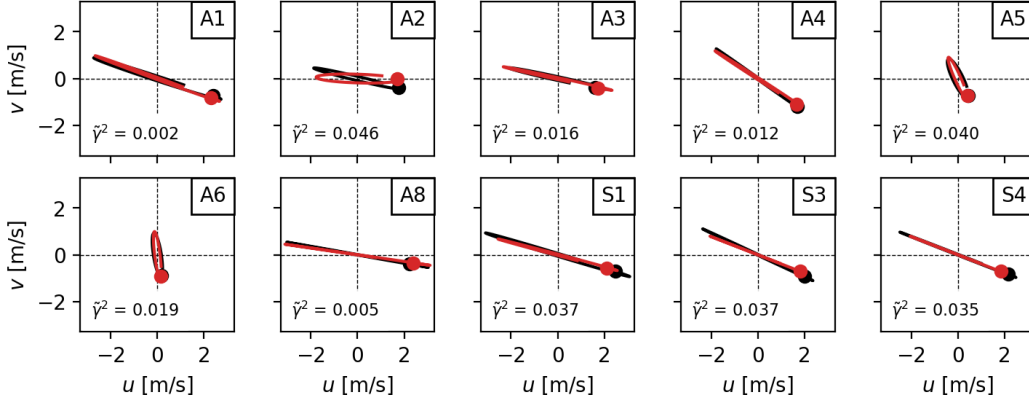


Figure 3. M_2 tidal ellipses of depth-averaged current at the 10 ADCP locations shown in Figure 1c. The ellipses for observations and predictions by CTRL are shown in black and red, respectively. The last 10th of the tidal cycle is omitted to indicate the sense of rotation. The dot shows the initial time. $\tilde{\gamma}^2$ for each station is given in the lower left corner of each panel. The speeds are in m s^{-1} .

428 in Minas Passage (locations A1–A4, A8, and S1–S3) with speeds exceeding 3 m s^{-1} . In-
 429 side Minas Basin (A5 and A6), the currents are weaker with maximum M_2 speeds of about
 430 1 m s^{-1} . Based on visual comparison, the predictions are in good agreement with the ob-
 431 servations and this is confirmed by the low values of $\tilde{\gamma}^2$ for each location given in the lower
 432 left corner of each panel. Combining results for all ADCP locations, $\tilde{\gamma}^2 = 0.023$. This
 433 is a slight improvement over WebTide ($\tilde{\gamma}^2 = 0.034$) and a significant improvement over
 434 GoMSS ($\tilde{\gamma}^2 = 0.201$, see Table 2).

435 As a further check on the model, predictions of tidal elevation for S_2 and N_2 were
 436 also compared to observations. The $\tilde{\gamma}^2$ values (Table 2) show the performance of CTRL
 437 is comparable to WebTide, and slightly better than GoMSS.

438 Summarizing the results of this subsection, UBoF provides good predictions of M_2 tidal
 439 elevations and currents in the study region.

440 5.2 M_4 Elevation

441 The M_4 amplitude and phase of elevation predicted by CTRL are shown in Fig-
 442 ure 4. The largest amplitudes are predicted for Cobequid Bay reaching 1.44 m at the head (x_H).
 443 Unfortunately, no observations are available for this region. In the Avalon River (Fig-

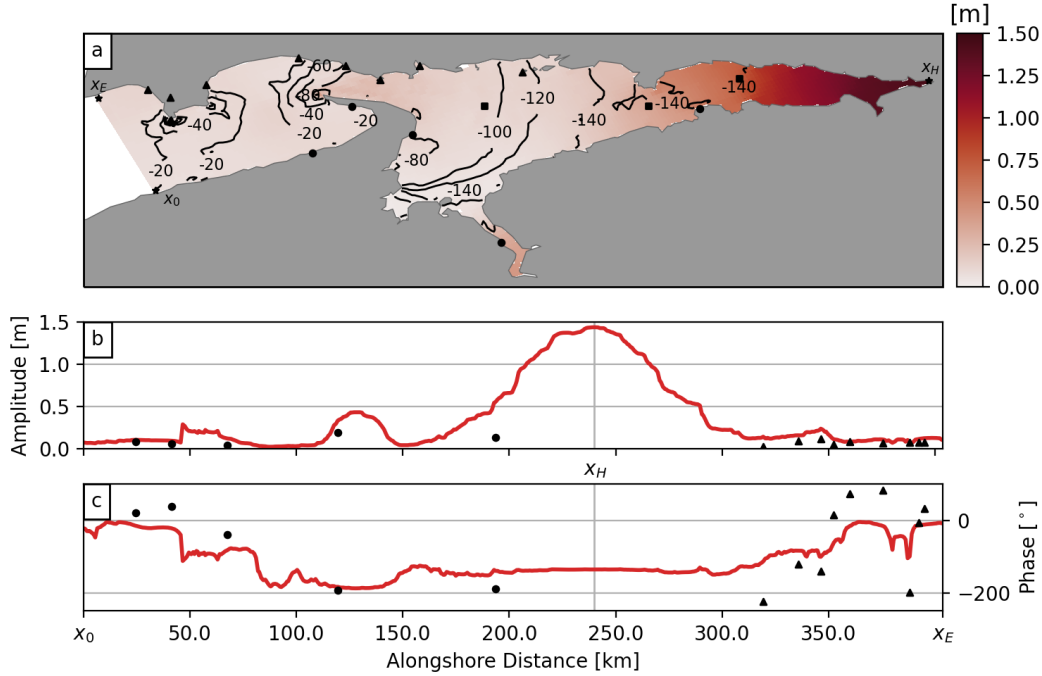


Figure 4. Predicted and observed amplitude and phase of M_4 tidal elevation. The format is the same as Figure 2.

444 ure 1b), M_4 amplitudes reach 0.43 m. At Cape Split and in Minas Passage, CTRL pre-
 445 dicts amplitudes of 0.41 m and 0.26 m, respectively. These local maxima can be explained
 446 by the Bernoulli effect as well as vorticity generation and subsequent advection due to
 447 the strong tidal currents through the narrow strait (see Section 2.1).

448 The phase mapped in Figure 4a suggests the M_4 oscillations in the upper reaches
 449 of Cobequid Bay and the Avalon River are standing (see also Figure 4c). Beyond these
 450 two regions the phase suggests propagation as a shallow water wave toward the open bound-
 451 ary.

452 The alongshore variation of observed and predicted M_4 tidal elevation at the coast
 453 is shown in Figures 4b and c. It is clear that the overall agreement at the 14 coastal tide
 454 gauges is poor, e.g., the predicted amplitudes are generally too large, and the phase changes
 455 in the vicinity of Minas Passage are too small. This poor agreement is confirmed by large
 456 RMSEs of 0.12 m and 65.1° for M_4 amplitude and phase and $\tilde{\gamma}^2 = 3.3$. Adding obser-
 457 vations from the three bottom pressure gauges (squares in Figure 4a) gives combined RM-
 458 SEs for amplitude and phase of 0.19 m and 62.6° and $\tilde{\gamma}^2 = 5.6$. Clearly, CTRL has no

Table 3. Observed and predicted amplitude and phase for M_4 elevation at the three bottom pressure gauges (squares in Figure 1b). M_4/M_2 is the amplitude ratio and $2\theta_{M_2} - \theta_{M_4}$ is the phase of M_4 relative to M_2 at the same location. The row order of the stations is from west to east.

Station		M_4 Amp. [m]	M_4 Phase [°]	M_4/M_2	$2\theta_{M_2} - \theta_{M_4}$ [°]
40258	Observations	0.01	-55.1	0.002	296.8
	UBoF CTRL	0.12	-94.0	0.022	333.3
	WebTide	0.12	-134.1	0.023	383.1
40262	Observations	0.09	162.0	0.016	88.9
	UBoF CTRL	0.35	-144.6	0.063	401.5
	WebTide	0.25	-156.6	0.044	416.7
40264	Observations	0.18	164.6	0.029	94.1
	UBoF CTRL	0.72	-141.1	0.125	412.6
	WebTide	0.41	-157.9	0.069	427.9

459 skill in predicting M_4 elevation at the coast (Table 2). WebTide also performs poorly
 460 with RMSEs for amplitude and phase of 0.10 m and 74.6° and $\tilde{\gamma}^2 = 1.8$ (Table 2).

461 The M_2 and M_4 amplitude and phase at the three offshore bottom pressure loca-
 462 tions (squares in Figure 1b, Table 3) are now examined. At the most western gauge in
 463 Minas Basin (40258), the predicted M_4 amplitude is 0.12 m which corresponds to an M_4/M_2
 464 amplitude ratio of 0.022. The observed M_4 amplitude at this location is 0.01 m and the
 465 observed M_4/M_2 amplitude ratio is only 0.002. Moving toward the head of the basin,
 466 both the model and observations show an increase in M_4 , however the predicted ampli-
 467 tude at the eastern most gauge in Cobequid Bay (40264) is four times larger than ob-
 468 served (Table 3). This discrepancy is also reflected in the observed and predicted M_4/M_2
 469 ratios at that station.

470 The observed and predicted M_4 phases at the three bottom pressure locations sug-
 471 gest a standing M_4 oscillation in Cobequid Bay, and westward propagation away from
 472 this region (Table 3). Differences exist however in the M_4 phase relative to the M_2 tide.
 473 At the two eastern bottom pressure gauges, the observed relative phase $2\theta_{M_2} - \theta_{M_4} \approx$

474 90° which indicates flood dominance with maximum asymmetry between a short flood
 475 period with strong currents and longer ebb duration with weaker currents (Friedrichs &
 476 Aubrey, 1988). This flood dominance is also predicted by CTRL, however, the tidal dis-
 477 tortion is less pronounced compared to the observations ($2\theta_{M_2} - \theta_{M_4} = 53^\circ$ for the east-
 478 ern station in Cobequid Bay, 40264). The presence of tidal flats, which are prevalent in
 479 this region, can have significant influence on the distortion of the tidal wave (e.g., Speer
 480 & Aubrey, 1985). This is not captured in UBoF because it does not include wetting and
 481 drying.

482 The above discussion leads us to speculate that the M_4 tide predicted by UBoF is
 483 contaminated by an unrealistically large signal that is generated in Cobequid Bay and
 484 subsequently propagates westward toward the open boundary. To test this speculation,
 485 the predictions of M_4 tidal elevation at all 11 tide gauges to the west of bottom pres-
 486 sure gauge 40258 (henceforth the reference station) were corrected as follows:

$$487 \quad A'_j = A_j - A_{\text{ref}} \exp \left[i\Delta\theta \left(\frac{\lambda_j - \lambda_{\text{ref}}}{\lambda_0 - \lambda_{\text{ref}}} \right) \right], \quad \text{with } j = 1, \dots, 11, \quad (9)$$

488 where A_j is the complex M_4 amplitude at the j th tide gauge and A_{ref} is the complex M_4
 489 amplitude at the reference station. λ_j , λ_{ref} and λ_0 are the longitudes of the j th tide gauge,
 490 the reference station, and the most western tide gauge (235), respectively. The only free
 491 parameter in (9) is $\Delta\theta$, the spatial change in phase associated with a shallow water wave
 492 propagating at constant speed from the reference station to the open boundary. The op-
 493 timal value was determined by minimizing $\tilde{\gamma}^2$ and corresponded to a time lag of 1.0 h,
 494 implying a phase speed of 13 m s^{-1} .

495 Equation (9) was used to correct the observed and predicted M_4 amplitudes and
 496 phases of tidal elevation. The resulting $\tilde{\gamma}^2$ are listed in Table 4. The correction signif-
 497 icantly improves the model fit of CTRL at all but one station and thus supports the spec-
 498 ulation that the large M_4 error is generated remotely in Cobequid Bay. This example
 499 clearly highlights a potential problem with using M_4 elevation for model validation; the
 500 fit at a given location can be dominated by remotely generated errors. The spatial ref-
 501 erencing technique outlined above is one way of overcoming this limitation and extract-
 502 ing useful information from M_4 elevations for validation.

Table 4. $\tilde{\gamma}^2$ for original and corrected predictions of M_4 elevation at coastal tide gauges (see Figure 1b). The corrections were made using (9). All stations are west of the reference bottom pressure gauge 40258. See text for details.

Station	CTRL	CTRL corr.	WebTide	WebTide corr.
235	1.484	0.161	0.177	2.584
236	0.328	1.082	0.499	5.070
240	2.224	0.151	1.370	0.935
242	3.953	0.180	1.754	0.191
245	1.892	0.019	0.677	0.329
247	4.143	0.472	7.159	1.010
250	1.829	0.202	1.343	0.371
255	1.285	0.484	0.581	0.389
290	4.475	0.891	8.683	2.241
300	2.204	0.461	1.241	1.340
305	0.569	0.358	0.810	1.062

5.3 M_4 Currents

The M_4 tidal ellipses calculated from observed and predicted depth-averaged currents are shown in Figure 5. The $\tilde{\gamma}^2$ values are given in the lower left corner of each panel. Both observations and predictions agree that the strongest M_4 currents occur in Minas Passage (A1–A4, A8, and S1–S3) where speeds approach 0.3 m s^{-1} . Inside Minas Basin (A5 and A6), the currents are much weaker and $\mathcal{O}(0.1 \text{ m s}^{-1})$.

Generally, locations with strong observed M_4 currents also have strong M_4 predictions. The only exception is A2. The individual values of $\tilde{\gamma}^2$ show the model has skill in predicting M_4 currents at most locations. For all ADCP stations combined, $\tilde{\gamma}^2 = 0.329$ which is comparable to WebTide ($\tilde{\gamma}^2 = 0.325$, see Table 2). These values of $\tilde{\gamma}^2$ indicate better prediction of M_4 current than M_4 tidal elevation.

As discussed in Section 2, both nonlinear advection and bottom friction can generate overtides. As a result, strong M_4 currents are often observed around headlands (Geyer & Signell, 1990) and in regions where strong M_2 currents vary on small spatial scales (Davies

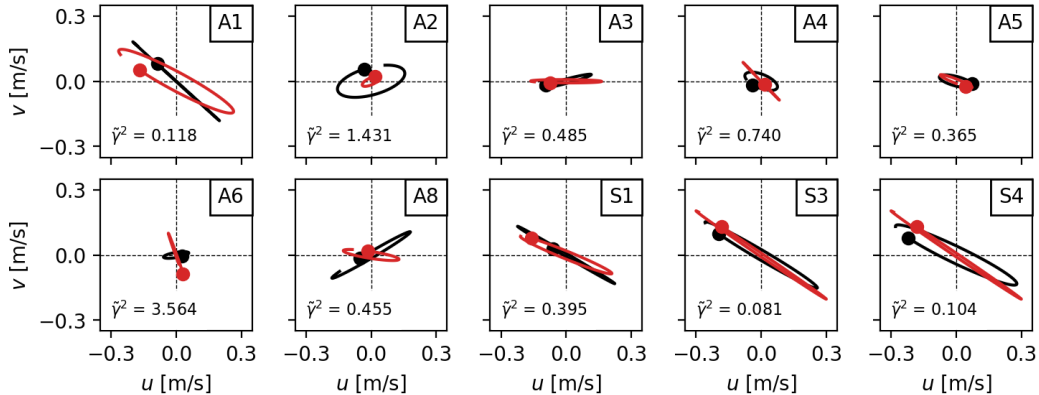


Figure 5. Predicted (red) and observed (black) M_4 tidal ellipses of depth-averaged currents. The format is the same as in Figure 3.

517 & Lawrence, 1994). In the previous section it was shown that the strongest M_2 currents
 518 are observed (and predicted) in Minas Passage. This results in flow separation at Cape
 519 Split and Cape Blomidon, an asymmetry in the flow pattern between flood and ebb (Tee,
 520 1976), and strong M_4 currents on either side of these two promontories (Mardell & Pin-
 521 gree, 1981; Geyer & Signell, 1990).

522 There is no obvious relationship between the orientation of the M_4 and M_2 cur-
 523 rents (cf. Figures 3 and 5). However, it will be shown in the next section that both the
 524 predicted and observed M_4 currents are closely aligned with the mean circulation. This
 525 is in agreement with the figures presented by Hasegawa et al. (2011).

526 5.4 Mean Currents

527 The streamlines of the predicted time-averaged depth-mean currents are shown in
 528 Figure 6a. The residual circulation is strongest in and around Minas Passage where four
 529 permanent eddies can be seen (I–IV). Overall, this circulation is in qualitative agreement
 530 with previous studies (e.g., Tee, 1976, 1977; Greenberg, 1983; Hasegawa et al., 2011; Wu
 531 et al., 2011). The four permanent eddies have already been identified and explained by
 532 Tee (1976) based on vorticity arguments, idealized model simulations, and runs with more
 533 realistic bathymetry and coastline. He showed that the eddies are due to the combined
 534 effect of vorticity generation close to shore, subsequent advection by the tidal flow and
 535 non-local dissipation (see Section 2.1). Averaging over a tidal cycle results in the four

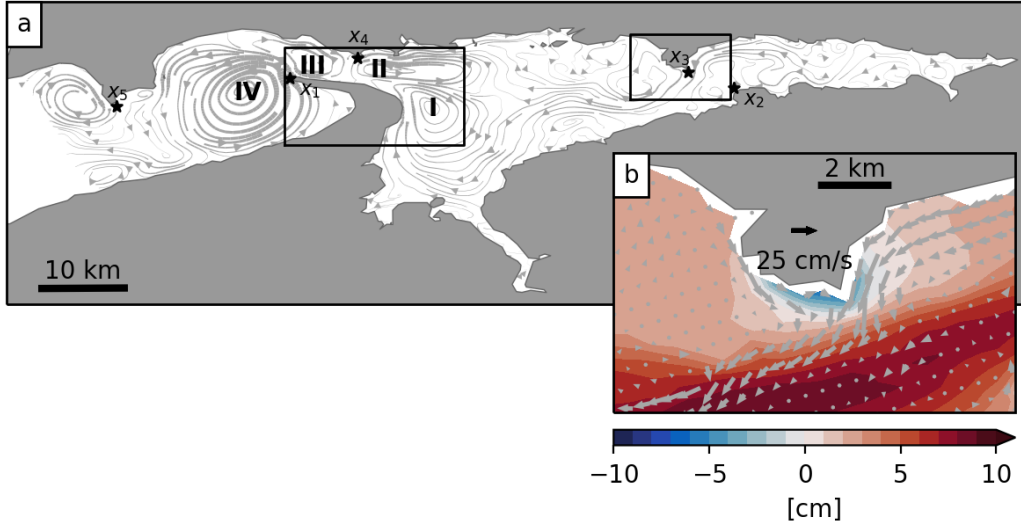


Figure 6. Predicted time mean of depth-averaged currents. (a) Streamlines predicted by CTRL. (b) Predicted mean circulation around the headland at x_3 . Colors show the predicted MDT with the Bernoulli setdown removed.

536 permanent eddies described above. Tee (1976) also showed that the four eddies are due
 537 to the particular geometry of Minas Passage and Basin; he found no significant changes
 538 on setting the bathymetry to a constant value throughout the model domain, or reduc-
 539 ing the size of Cobequid Bay to simulate removal of the mudflats that exist in the up-
 540 per part of the Bay.

541 Figure 7 is an enlarged view of the mean flow in Minas Passage with the predicted
 542 mean flow now shown as grey vectors at every model grid point. Black vectors show the
 543 time mean of the observed depth-averaged currents calculated at the ten ADCP stations.
 544 Overall, this circulation pattern is in agreement with the observations. The model pre-
 545 diction is also consistent with additional observations made by current meters (Tee, 1977)
 546 which are not shown here.

547 To quantify the model fit, we calculated $\bar{\gamma}^2$ using the model predictions at the grid
 548 points closest to the observation locations. The resulting values are given in Table 5. There
 549 is general agreement between the observed and predicted mean currents at the 10 loca-
 550 tions with the overall $\bar{\gamma}^2 = 0.303$. The reason for the large values of $\bar{\gamma}^2$ at some sites
 551 is a slight misplacement of the eddies in the model with respect to the observations (see

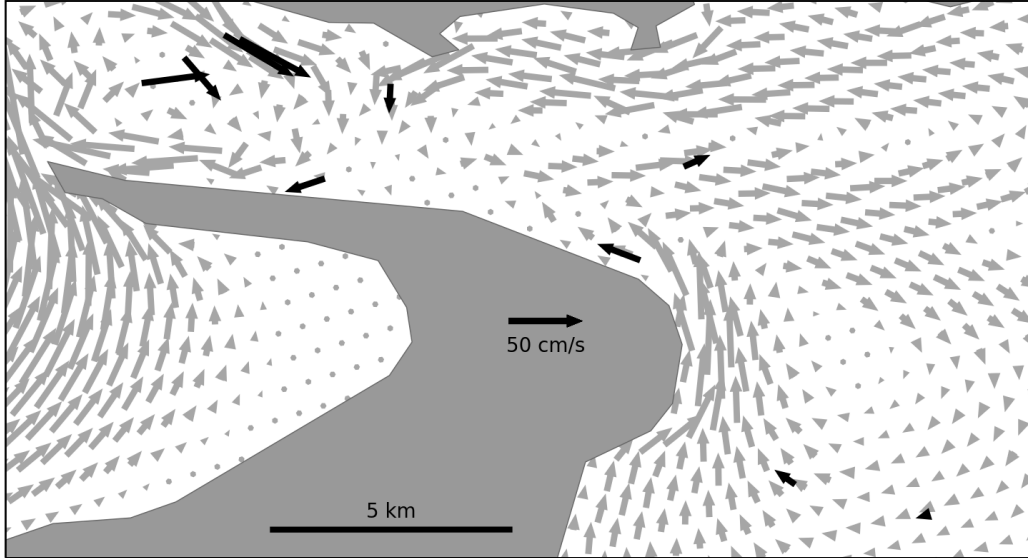


Figure 7. Predicted and observed time mean of depth-averaged currents around Cape Split. Black vectors show the observations at the 10 ADCP locations shown in Figure 1c.

Table 5. $\bar{\gamma}^2$ for the predicted time mean of depth-averaged currents at grid points closest to the 10 ADCP locations.

A1	A2	A3	A4	A5	A6	A8	S1	S3	S4
0.000	0.577	0.080	0.210	0.017	0.101	0.972	0.426	0.058	0.061

552 Figure 7). It is important to note that for GoMSS the fit to the mean currents is sig-
 553 nificantly worse ($\bar{\gamma}^2 = 0.876$, Table 2). Mean currents from WebTide were not available.

554 In addition to the basin scale circulation, UBoF is also able to capture localized
 555 features that are generated by tidal flow around headlands. Figure 6b is a zoom of the
 556 predicted mean around the headland at x_3 . On either side of the headland, a pair of counter-
 557 rotating eddies can be identified which join to form a strong mean offshore flow away from
 558 the tip. As discussed in Section 2.1, this is the result of vorticity generation caused by
 559 the tidal flow past the headland, followed by flow separation and non-local vorticity dis-
 560 sipation.

561 Overall, the above model validation shows that UBoF can predict the tides and mean
 562 currents in the upper Bay of Fundy including the nonlinear interactions that lead to over-

563 tides and the mean circulation. This increases our confidence in the predictions of MDT
 564 which will be discussed in the following section.

565 **6 Mean Dynamic Topography**

566 In this section, we present the MDT in the upper Bay of Fundy predicted by CTRL
 567 and use the information about overtides to explain the differences in the MDT predic-
 568 tions by UBoF and GoMSS. The discussion focuses on the role of horizontal resolution
 569 and bathymetry which have the largest impact on the predicted MDT. The choice of model
 570 parameters for bottom and lateral friction has little effect (see “S” runs in Table 2 and
 571 Appendix A).

572 **6.1 Prediction of MDT from UBoF**

573 The MDT predicted by CTRL is shown in Figure 8. The dominant feature is the
 574 drop of almost 0.4 m in Minas Passage which can be explained by the Bernoulli effect
 575 and the strong M_2 currents (see Section 2.1). This explanation is supported by the sim-
 576 ilar amplitude of M_4 elevation in this region (Figure 4b). More localized drops of MDT
 577 can also be seen around Cape Split and several headlands (e.g., x_3 , x_4 , and x_5). To quan-
 578 tify the MDT on the larger scale, we use the alongshore difference between locations A
 579 and B defined by $\Delta\bar{\eta} = \bar{\eta}_A - \bar{\eta}_B$. These locations were chosen to minimize the effect
 580 of local processes around headlands. From Figure 8 it is clear that the MDT inside Mi-
 581 nas Basin is higher than in Minas Channel with $\Delta\bar{\eta} = 2.6$ cm.

582 The predicted MDT after correction for the Bernoulli effect is shown in Figure 9.
 583 This correction reduces the overall variability, but $\Delta\bar{\eta}$ remains positive (equal to 2.0 cm)
 584 and local depressions of MDT remain in the vicinity of Cape Split and the headlands men-
 585 tioned above. At the head of Cobequid Bay a small setdown is predicted.

586 In order to explain this setdown, the Li and O’Donnell (2005) channel model (see
 587 Section 2.2) was extended to allow for forcing with multiple tidal constituents. If the tidal
 588 wave prescribed at the open boundary is the sum of a main tidal constituent and its first
 589 harmonic, e.g., M_2 and M_4 , the model can predict a setdown in mean sea level toward
 590 the end of the channel (not shown). This setdown can be explained in terms of the asym-
 591 metry in the forcing due to the inclusion of the overtide. More specifically, the predicted
 592 tidal wave entering Cobequid Bay has a significant M_4 amplitude (0.72 m at the west-

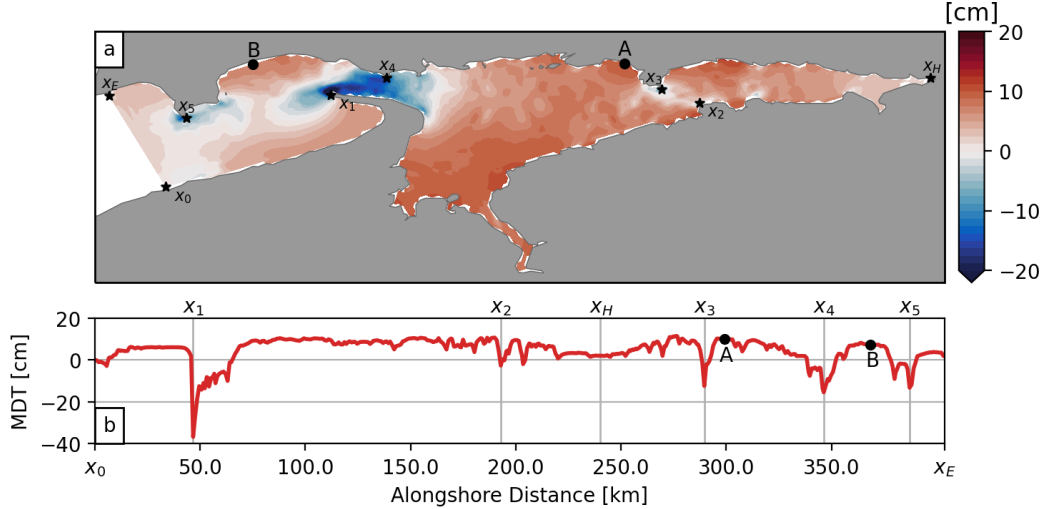


Figure 8. MDT relative to the value at x_0 predicted by CTRL. (a) Model prediction of MDT. Note that the minimum at Cape Split (-37 cm) is outside the range of the colorbar. The two black dots A and B indicate the model grid points used to calculate $\Delta\bar{\eta}$. Stars mark alongshore reference points. (b) Predicted MDT as a function of alongshore distance from x_0 .

ern most bottom pressure gauge 40264, see Table 3) resulting in a strong and short in-
 flow balanced by weaker and longer outflow. The net effect is a mean bottom stress that
 must be balanced by a pressure gradient leading to a setdown in mean sea level at the
 head (Pingree et al., 1984).

Figure 6b shows the Bernoulli-corrected MDT around the headland at x_3 . A set-
 down at the tip of the headland is evident. As discussed in Section 2, tidal flow around
 a headland generates not only a mean Bernoulli setdown, but also a flow toward the tip.
 Along the coast, a pressure gradient is required to drive the mean flow toward the tip
 of the headland. An analysis of the predicted momentum balance shows that this pres-
 sure gradient is primarily balanced by bottom friction. Note that the setdown shown in
 Figure 6b is consistent with the “back-of-the-envelope” calculation in Section 2.1 that
 showed frictional and Bernoulli contributions to the setdown at the tip can be compa-
 rable. There is also a secondary contribution from the time mean of the $\zeta\hat{\mathbf{k}} \times \mathbf{u}$ term
 in the momentum equation, associated with the transient eddies generated either side
 of the headland. (The use of an Arakawa C-grid means the model sea level is not exactly
 at the coast where the $\zeta\hat{\mathbf{k}} \times \mathbf{u}$ term vanishes.) The same momentum balance holds for
 the predicted MDT setdowns at Cape Split (x_1) and in Minas Passage (x_4).

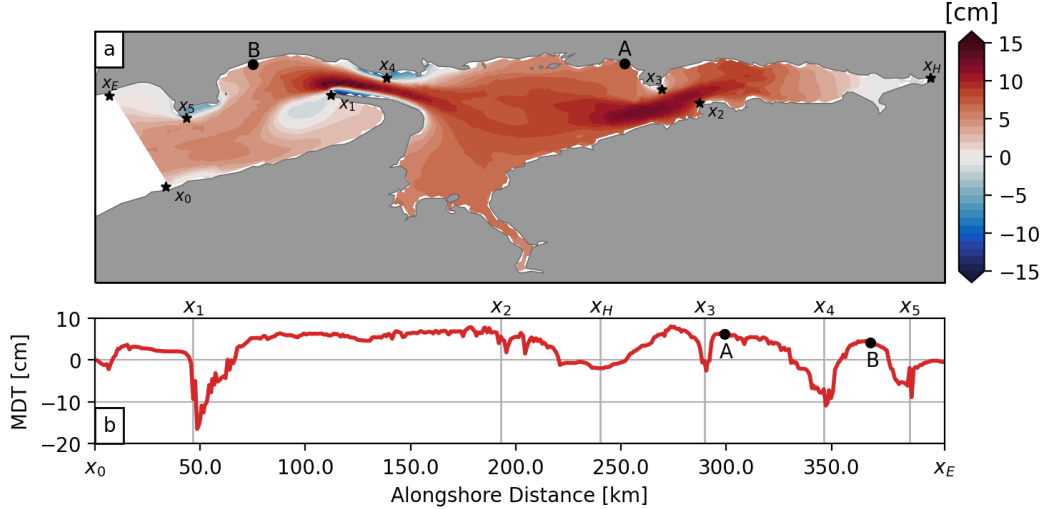


Figure 9. MDT prediction by CTRL with the mean Bernoulli setdown $-\overline{\mathbf{u}^2}/2g$ subtracted.

The format is the same as in Figure 8.

6.2 Using Observed Overtides to Identify Errors in Predicted MDT

We now explore the possibility of using overtides to assess the accuracy of MDT predictions. Particular attention is paid to the effect of spatial resolution and bathymetry, the most relevant differences between GoMSS and UBoF. As discussed in Section 5.2, none of the models considered here has skill in predicting M_4 elevation (Table 2) and therefore it has been excluded from the discussion below.

Figure 10 shows the joint variation of the alongshore tilt of MDT ($\Delta\bar{\eta}$, same for all panels) and γ^2 for different model runs. The MDT predicted by runs with poor fits to the observed overtides and mean currents will be considered unreliable.

GoMSS predicts a 6.1 cm setdown going into Minas Basin through Minas Passage. There is nothing in the fit of the observed and predicted M_2 elevations and currents that raises concern about the accuracy of this drop in mean sea level (Figures 10a and b). The corresponding plot for M_4 currents (Figure 10c) tells a different story: $\tilde{\gamma}^2$ is close to 2 indicating no predictive skill for the dominant overtide. Given the intrinsic relationship between MDT and overtides, this high value of γ^2 means that the GoMSS setdown must be considered suspect. This is further supported by the high value of $\bar{\gamma}^2$ for mean currents (Figure 10d).

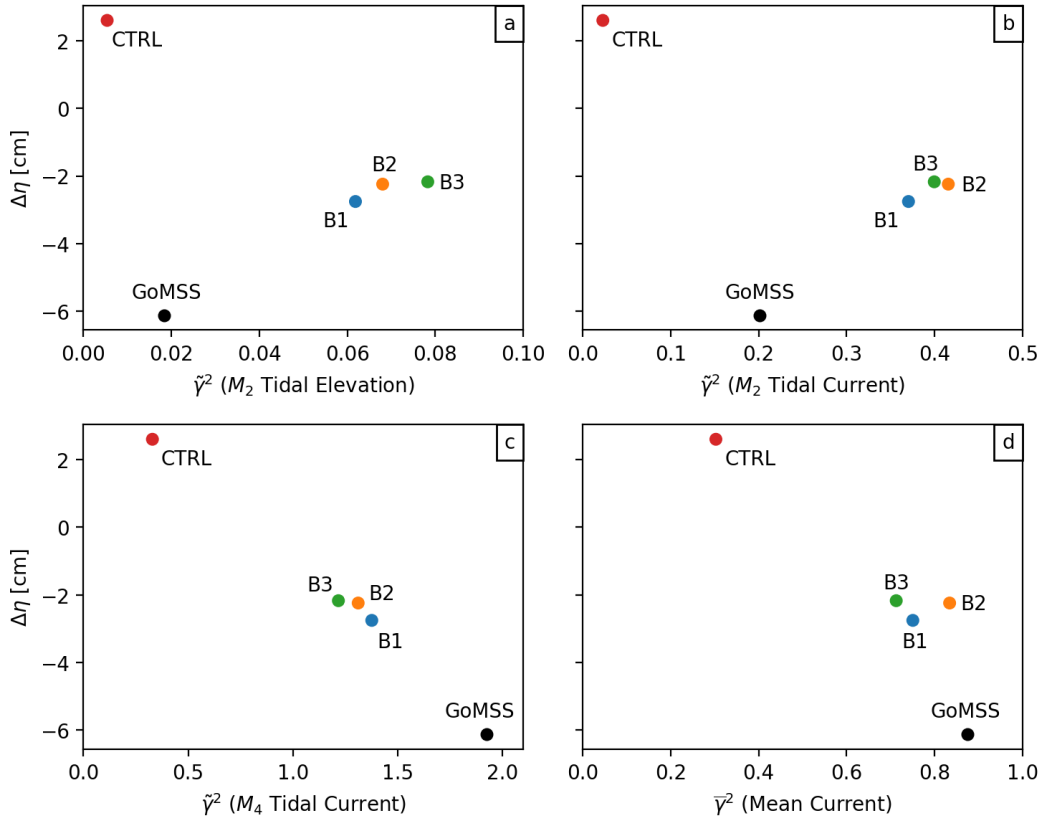


Figure 10. MDT difference $\Delta\bar{\eta}$ as a function of γ^2 for models with different horizontal resolution and bathymetry. The x -axis shows the following measures of model fit for (a) M_2 tidal elevation, (b) M_2 tidal current (c) M_4 tidal current and (d) mean current. Black dots show the results for GoMSS. Runs B1–B3 use the same high-resolution grid, model parameters, and forcing as CTRL, but the bathymetry is replaced by the GoMSS bathymetry using different interpolation schemes (see Table 1 for details). Note the range of the x -axis varies among the panels.

627 The values of $\Delta\bar{\eta}$ and γ^2 for CTRL are also shown in Figure 10 (red dots). This
 628 run of UBoF predicts a 2.6 cm setup of mean sea level. The low values of γ^2 for M_4 and
 629 mean currents provide strong support in favor of the CTRL prediction of a small setup
 630 of MDT, and not the 6.1 cm setdown predicted by GoMSS.

631 Why does CTRL provide more accurate predictions of the overtides and mean cur-
 632 rents at the ADCP locations? The CTRL configuration is superior to GoMSS in two re-
 633 spects: (i) its horizontal grid is refined by a factor of 4 compared to GoMSS, (ii) its bathymetry
 634 has been generated specifically for UBoF (Section 3.2). The runs B1–B3 were designed
 635 to assess the effect of (ii). They all have the same high-resolution grid and model param-
 636 eters as CTRL, and differ only in the way the GoMSS bathymetry was interpolated to
 637 the UBoF grid (Table 1). The values of $\Delta\bar{\eta}$ and $\tilde{\gamma}^2$ for the runs B1–B3 are shown in Fig-
 638 ure 10 (blue, orange and green dots).

639 In comparison to CTRL, the use of the interpolated GoMSS bathymetry in the runs
 640 B1–B3 degrades the model fit for all three interpolation schemes. In particular, for M_4
 641 and mean currents, the values of γ^2 are close to 1. This demonstrates the added value
 642 of the in-situ depth measurements that were used to create the bathymetry of CTRL.

643 Relative to GoMSS, the interpolated bathymetry in runs B1–B3 degrades the fit
 644 for M_2 elevation and currents. Note that the bathymetry in GoMSS was optimized to
 645 accurately capture the tides in the whole Bay of Fundy using tidal forcing along the open
 646 boundaries of that model (Dr. A. Katavouta, 2021, personal communication). No such
 647 tuning was done for runs B1–B3. This is the likely explanation for the higher skill of GoMSS
 648 in predicting the M_2 tide compared to runs B1–B3. Despite a small improvement of model
 649 fit for M_4 and mean currents relative to GoMSS, the values of γ^2 are close to 1 indicat-
 650 ing the B1–B3 runs are still unreliable.

651 The runs B1–B3 all predict $\Delta\bar{\eta}$ between -2 and -3 cm. This setdown is smaller
 652 than the GoMSS prediction, but still of opposite sign to the CTRL prediction. Based
 653 on the poor performance of runs B1–B3 in predicting overtides and the mean currents,
 654 these predicted setdowns have to be considered suspect.

655 Overall, the use of overtides leads to conclusion that the large setdown in MDT pre-
 656 dicted by GoMSS is highly suspect and the 2.6 cm setup predicted by the control run
 657 of UBoF is more realistic.

7 Summary and Discussion

The first step in this study of overtides was to show that the control run of our high-resolution model of the upper Bay of Fundy (UBoF) agrees well with the overwhelmingly dominant semi-diurnal tides observed in coastal sea level, bottom pressure and current. The skill of UBoF is comparable to WebTide, a data-assimilating tidal model that covers the Scotian Shelf and Gulf of Maine, and a significant improvement over GoMSS (Table 2). Good agreement was also found between observations of M_4 currents and predictions by UBoF and WebTide. Both models gave poor predictions of M_4 elevation. This was explained in terms of an error generated in the upper reaches of Cobequid Bay, related to the representation of wetting and drying in the models, that subsequently propagated throughout the model domains as a shallow water wave. A statistical method (“station referencing”) was developed to remove this remotely generated signal from the M_4 observations and predictions prior to validation, thereby allowing useful information to be extracted from the M_4 elevations. We anticipate this method has wider applicability to other regions. Using the tidally validated UBoF model, we next addressed the three research questions listed in the Introduction. Our answers are summarized and discussed below.

“Are observed overtides useful in specifying the bathymetry and parameters of ocean models?” In contrast to observations of the dominant semi-diurnal tide, overtides proved useful in selecting the most appropriate bathymetry for UBoF. It is based on a publicly-available, high-resolution gridded bathymetry (GEBCO) combined with approximately 10^5 in-situ measurements using a modified form of optimal interpolation. It is the most accurate of all the bathymetries examined in this study and gave the most skillful predictions of M_4 tidal and mean currents. The higher skill was explained by the more accurate representation of advection and nonlinear bottom friction.

Simply increasing the horizontal resolution of the gridded bathymetry of GoMSS did not lead to significant improvements in UBoF’s predictions of M_2 and M_4 tides or mean currents (see B1–B3 runs, Figure 10). This is at odds with Tee (1976) who showed that setting the bathymetry to a constant value does not have a significant effect on the prediction of the mean circulation of the study region. We conclude, based on model validation using observations at multiple frequencies including overtides, that a realistic bathymetry is critical.

690 Based on a set of sensitivity studies (see Appendix A)) we showed that, given the
 691 limited observations available for the study region, it is challenging to define a “best”
 692 set of model parameters for UBoF. However, validation using overtides does provide use-
 693 ful information that leads to stronger constraints on the model parameters. It also in-
 694 creases confidence in the representation of nonlinear processes (e.g. Pingree & Maddock,
 695 1978).

696 *“Are observed overtides useful in validating predicted MDT?”* The control run of
 697 UBoF predicts a mean sea level difference between Minas Basin and Minas Channel of
 698 $\Delta\bar{\eta} = 2.6$ cm. This setup has the opposite sign, and smaller magnitude, than the cor-
 699 responding prediction by GoMSS ($\Delta\bar{\eta} = -6.1$ cm). Based on the poor predictions of M_4
 700 current and mean current by GoMSS (Table 2), its MDT prediction should also be con-
 701 sidered suspect. The skillful predictions of M_4 current and mean current by UBoF show
 702 that this model has captured the dominant nonlinear processes in this tidally-dominated
 703 region, thereby increasing our confidence in its prediction of MDT.

704 *“Are observed overtides useful in the design of geodetic and ocean observing sys-
 705 tems?”* From a geodesist’s perspective, a high resolution ocean model, validated using
 706 observed overtides and mean currents, can provide guidance in future deployments of tide
 707 gauges in support of geoid model validation. Predictions by such models can be used to
 708 identify, and thus avoid, regions with highly localized features in MDT that exceed the
 709 standard error of the most recent generation of geoid models (<3 cm, Huang, 2017). For
 710 example, tidal flow around headlands can result in local setdowns of coastal MDT of or-
 711 der $\mathcal{O}(10$ cm) resulting from the combined effect of Bernoulli setdown and the pressure
 712 gradient required to balance the mean bottom stress along the coast. Bernoulli setdowns
 713 of similar order are also possible in narrow tidal channels like Minas Passage.

714 From an oceanographer’s perspective, the two main advantages of using overtides
 715 to validate an ocean model’s MDT (and hence its mean state) are (i) the observed record
 716 can be relatively short, i.e., $\mathcal{O}(1$ month) and (ii) its vertical datum does not need to be
 717 specified. Reliable observations of mean sea level for MDT validation using the standard
 718 geodetic approach require hourly records that are at least several decades in length with
 719 continuous vertical datum control (Woodworth et al., 2012). On the negative side, pre-
 720 dictions of overtides in sea level can be contaminated by remotely generated errors and
 721 care must be taken in the selection of coastal tide gauges and offshore bottom pressure

sensors in order to minimize such errors. If the errors propagate as a shallow water wave, their remote effect will have a relatively weak signature in currents compared to sea level. This implies that, in some regions, observed overtides in currents may be more useful than overtides in sea level for model validation.

Appendix A Sensitivity of γ^2 and $\Delta\bar{\eta}$ to Variations of c_d and A_h^m

Multiple runs of UBoF were performed to assess the impact of changing model parameters related to energy dissipation by bottom friction, horizontal and vertical mixing, and the formulation of the coastal boundary condition. The most important parameters were found to be the minimum bottom friction coefficient (c_d) and the background lateral eddy viscosity coefficient (A_h^m).

The effect on model fit (γ^2) of systematically varying c_d and A_h^m over a realistic range, keeping all other model parameters fixed as in CTRL, is given by the “S” runs values in Table 2. Overall, the effect on tidal elevation and current at semi-diurnal frequencies is small. None of the “S” runs has useful predictive skill for sea level variations at the M_4 frequency ($\tilde{\gamma}^2 > 1$) for the reasons given in Section 5.2. However, as detailed below, varying c_d and A_h^m does have a significant effect on M_4 tidal current and the mean current.

Figure A1 shows γ^2 (upper panels) and $\Delta\bar{\eta}$ (lower panels) as a function of c_d (left panels) and A_h^m (right panels). In all panels, the star shows the parameter value used in CTRL. Reducing c_d and A_h^m improves the fit to the observed mean current (red lines). The reason is that all of the UBoF runs generally underestimate the speed of the mean current (not shown) and reducing c_d and so A_h^m leads to faster mean currents and a better fit to the observations. The effect of reducing c_d and A_h^m on the fit to M_4 tidal current (blue lines) is more subtle but it is clear that the worst fits are found for the smaller parameter values. This can be explained by an overestimation of the M_2 tidal currents and, as a result, an overestimation of the M_4 currents at low parameter values. These sensitivity studies show that it is not possible to clearly define a “best” set of model parameters. This is discussed in Section 7.

The lower panels of Figure A1 show that the predicted large-scale MDT, as measured by $\Delta\bar{\eta}$, is insensitive to changes in c_d and A_h^m over realistic ranges with $2.4 \text{ cm} < \Delta\bar{\eta} < 2.8 \text{ cm}$.

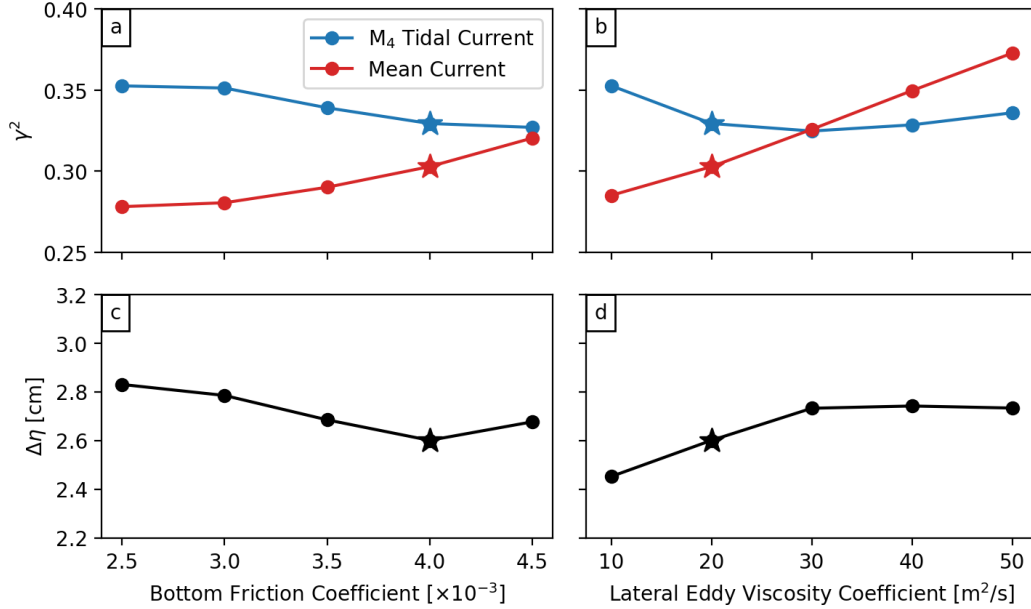


Figure A1. γ^2 and $\Delta\bar{\eta}$ as a function of bottom friction (a and c) and lateral eddy viscosity coefficient (b and d). The star indicates the UBoF control run (CTRL, see Table 1 for details).

Acknowledgments

All of the code and data required to configure and run the UBoF model are publicly available: NEMO source code (<https://www.nemo-ocean.eu/>), Webtide for open boundary conditions (<https://www.bio.gc.ca/science/research-recherche/ocean/webtide/index-en.php>), GEBCO for high-resolution gridded bathymetry (<https://www.gebco.net/>), and supplementary in-situ bathymetric observations from the Canadian Hydrographic Service. The sea level, bottom pressure and current observations were obtained from individuals and the Marine Environmental Data Section Archive at the Department of Fisheries and Oceans Canada (<https://meds-sdmm.dfo-mpo.gc.ca>) as described in the text. This work was funded by the Marine Environmental Observation, Prediction and Response (MEOPAR) Network of Canada. CR acknowledges funding from Nova Scotia Graduate Research Scholarship. KRT acknowledges support through the NSERC Discovery Grant program. The authors thank Anna Katavouta, David Greenberg, Shannon Nudds, and Yongsheng Wu for their support and encouragement.

References

Aubrey, D. G., & Speer, P. E. (1985). A Study of Non-linear Tidal Propagation in

- 769 shallow Inlet/Estuarine Systems Part I: Observations. *Estuarine, Coastal and*
 770 *Shelf Science*, *21*, 185–205.
- 771 Chassignet, E. P., Hurlburt, H. E., Smedstad, O. M., Halliwell, G. R., Hogan, P. J.,
 772 Wallcraft, A. J., . . . Bleck, R. (2007). The HYCOM (HYbrid Coordinate
 773 Ocean Model) data assimilative system. *Journal of Marine Systems*, *65*(1-4),
 774 60–83. doi: 10.1016/J.JMARSYS.2005.09.016
- 775 Davies, A. M., & Lawrence, J. (1994). A three-dimensional model of the M₄
 776 tide in the Irish Sea: The importance of open boundary conditions and in-
 777 fluence of wind. *Journal of Geophysical Research*, *99*(C8), 16197. doi:
 778 10.1029/94JC00480
- 779 Dupont, F., Hannah, C. G., & Greenberg, D. A. (2005). Modelling the sea level of
 780 the upper Bay of Fundy. *Atmosphere-Ocean*, *43*(1), 33–47. doi: 10.3137/ao
 781 .430103
- 782 Friedrichs, C. T., & Aubrey, D. G. (1988). Non-linear Tidal Distortion Estuaries in
 783 Shallow Well-mixed Estuaries: A Synthesis. *Estuarine, Coastal and Shelf Sci-*
 784 *ence*, *27*(5), 521–545. doi: 10.1016/0272-7714(88)90082-0
- 785 Garrett, C. (1972). Tidal Resonance in the Bay of Fundy and Gulf of Maine. *Na-*
 786 *ture*, *238*(5365), 441–443. doi: 10.1038/238441a0
- 787 Geyer, W. R., & Signell, R. (1990). Measurements of tidal flow around a headland
 788 with a shipboard acoustic Doppler current profiler. *Journal of Geophysical Re-*
 789 *search*, *95*(C3), 3189. doi: 10.1029/JC095iC03p03189
- 790 Greenberg, D. A. (1969). Modification of the M₂ Tide due to Barriers in the Bay of
 791 Fundy. *Journal of the Fisheries Research Board of Canada*, *26*(11), 2775–2783.
 792 doi: 10.1139/f69-274
- 793 Greenberg, D. A. (1983). Modeling the Mean Barotropic Circulation in the Bay of
 794 Fundy and Gulf of Maine. *Journal of Physical Oceanography*, *13*(5), 886–904.
 795 doi: 10.1175/1520-0485(1983)013<0886:MTMBCI>2.0.CO;2
- 796 Hasegawa, D., Sheng, J., Greenberg, D. A., & Thompson, K. R. (2011). Far-field
 797 effects of tidal energy extraction in the Minas Passage on tidal circulation in
 798 the Bay of Fundy and Gulf of Maine using a nested-grid coastal circulation
 799 model. *Ocean Dynamics*, *61*(11), 1845–1868. doi: 10.1007/s10236-011-0481-9
- 800 Higginson, S., Thompson, K. R., Woodworth, P. L., & Hughes, C. W. (2015). The
 801 tilt of mean sea level along the east coast of North America. *Geophysical Re-*

- 802 *search Letters*, 42(5), 1471–1479. doi: 10.1002/2015GL063186
- 803 Huang, J. (2017). Determining Coastal Mean Dynamic Topography by Geodetic
804 Methods. *Geophysical Research Letters*, 44(21), 11,125–11,128. doi: 10.1002/
805 2017GL076020
- 806 Hughes, C. W., & Bingham, R. J. (2006). An oceanographer’s guide to GOCE and
807 the geoid. *Ocean Science Discussions*, 3(5), 1543–1568.
- 808 Hughes, C. W., Fukumori, I., Griffies, S. M., Huthnance, J. M., Minobe, S., Spence,
809 P., ... Wise, A. (2019). Sea Level and the Role of Coastal Trapped Waves
810 in Mediating the Influence of the Open Ocean on the Coast. *Surveys in Geo-*
811 *physics*, 40(6), 1467–1492. doi: 10.1007/s10712-019-09535-x
- 812 Karsten, R. H., McMillan, J. M., Lickley, M. J., & Haynes, R. D. (2008). Assess-
813 ment of tidal current energy in the Minas Passage, Bay of Fundy. *Proceedings*
814 *of the Institution of Mechanical Engineers, Part A: Journal of Power and*
815 *Energy*, 222(5), 493–507. doi: 10.1243/09576509JPE555
- 816 Katavouta, A., & Thompson, K. R. (2016). Downscaling ocean conditions with ap-
817 plication to the Gulf of Maine, Scotian Shelf and adjacent deep ocean. *Ocean*
818 *Modelling*, 104(Supplement C), 54–72. doi: 10.1016/j.ocemod.2016.05.007
- 819 Katavouta, A., Thompson, K. R., Lu, Y., & Loder, J. W. (2016). Interaction be-
820 tween the Tidal and Seasonal Variability of the Gulf of Maine and Scotian
821 Shelf Region. *Journal of Physical Oceanography*, 46(11), 3279–3298. doi:
822 10.1175/JPO-D-15-0091.1
- 823 Lentz, S. J., & Fewings, M. R. (2012). The Wind- and Wave-Driven Inner-Shelf
824 Circulation. *Annual Review of Marine Science*, 4(1), 317–343. doi: 10.1146/
825 annurev-marine-120709-142745
- 826 Le Provost, C. (1991). Generation of Overtides and Compound Tides (Review). In
827 B. B. Parker (Ed.), *Tidal hydrodynamics* (pp. 269–295). Wiley.
- 828 Levier, B., Tréguier, A.-M., Madec, G., & Garnier, V. (2007). *Free surface and vari-*
829 *able volume in the NEMO code* (Tech. Rep.). Brest: Ifremer.
- 830 Li, C., & O’Donnell, J. (1997). Tidally driven residual circulation in shallow es-
831 tuaries with lateral depth variation. *Journal of Geophysical Research: Oceans*,
832 102(C13), 27915–27929. doi: 10.1029/97JC02330
- 833 Li, C., & O’Donnell, J. (2005). The Effect of Channel Length on the Residual Cir-
834 culation in Tidally Dominated Channels. *Journal of Physical Oceanography*,

- 835 35(10), 1826–1840. doi: 10.1175/JPO2804.1
- 836 Lin, H., Thompson, K. R., Huang, J., & Véronneau, M. (2015). Tilt of mean sea
837 level along the Pacific coasts of North America and Japan. *Journal of Geo-*
838 *physical Research: Oceans*, 120(10), 6815–6828. doi: 10.1002/2015JC010920
- 839 Lyard, F., Lefevre, F., Letellier, T., & Francis, O. (2006). Modelling the global
840 ocean tides: Modern insights from FES2004. *Ocean Dynamics*, 56(5-6), 394–
841 415. doi: 10.1007/s10236-006-0086-x
- 842 Madec, G., Romain, B.-B., Pierre-Antoine, B., Clément, B., Diego, B., Daley, C., ...
843 Martin, V. (2017). *NEMO ocean engine version 3.6 stable* (Tech. Rep. No. 27).
844 Paris: Pôle de modélisation de l’Institut Pierre-Simon Laplace (IPSL). doi:
845 10.5281/zenodo.1472492
- 846 Maraldi, C., Chanut, J., Levier, B., Ayoub, N., De Mey, P., Reffray, G., ... the
847 Mercator Research and Development Team (2013). NEMO on the shelf:
848 Assessment of the Iberia-Biscay-Ireland configuration. *Ocean Science*, 9(4),
849 745–771. doi: 10.5194/os-9-745-2013
- 850 Mardell, G. T., & Pingree, R. D. (1981). Half-wave rectification of tidal vorticity
851 near headlands as determined from current meter measurements. *Oceanologica*
852 *Acta*, 4(1), 63–68.
- 853 Munk, W. H. (1950). On the wind-driven ocean circulation. *Journal of Meteorology*,
854 7(2), 80–93. doi: 10.1175/1520-0469(1950)007<0080:OTWDOC>2.0.CO;2
- 855 Parker, B. B. (1991). The relative importance of the various nonlinear mechanisms
856 in a wide range of tidal interactions (Review). In B. B. Parker (Ed.), *Tidal Hy-*
857 *drodynamics* (pp. 237–268). Wiley.
- 858 Pingree, R. D., Griffiths, D. K., & Maddock, L. (1984). Quarter diurnal shelf
859 resonances and tidal bed stress in the English Channel. *Continental Shelf*
860 *Research*, 3(3), 267–289. doi: 10.1016/0278-4343(84)90012-8
- 861 Pingree, R. D., & Maddock, L. (1977). Tidal eddies and coastal discharge. *Journal*
862 *of the Marine Biological Association of the United Kingdom*, 57(03), 869. doi:
863 10.1017/S0025315400025224
- 864 Pingree, R. D., & Maddock, L. (1978). The M_4 tide in the English Channel derived
865 from a nonlinear model of the M_2 tide. *Deep-Sea Research*, 25(1), 53–63.
- 866 Proudman, J. (1953). *Dynamical Oceanography*. Methuen.
- 867 Robinson, I. (1983). Chapter 7: Tidally Induced Residual Flows. In B. Johns (Ed.),

- 868 *Physical Oceanography of Coastal and Shelf Seas* (Vol. 35, pp. 321–356). Else-
 869 vier. doi: 10.1016/s0422-9894(08)70505-1
- 870 Rodi, W. (1987). Examples of calculation methods for flow and mixing in strat-
 871 ified fluids. *Journal of Geophysical Research*, *92*(C5), 5305. doi: 10.1029/
 872 JC092iC05p05305
- 873 Saha, S., Moorthi, S., Pan, H.-L., Wu, X., Wang, J., Nadiga, S., . . . Goldberg, M.
 874 (2010). The NCEP Climate Forecast System Reanalysis. *Bulletin of the Amer-
 875 ican Meteorological Society*, *91*(8), 1015–1058. doi: 10.1175/2010BAMS3001.1
- 876 Signell, R. P., & Geyer, W. R. (1991). Transient eddy formation around headlands.
 877 *Journal of Geophysical Research: Oceans*, *96*(C2), 2561–2575. doi: 10.1029/
 878 90JC02029
- 879 Speer, P. E., & Aubrey, D. G. (1985). A Study of Non-linear Tidal Propagation in
 880 Shallow Inlet/Estuarine Systems Part II: Theory. *Estuarine, Coastal and Shelf
 881 Science*, *12*, 207–224.
- 882 Speer, P. E., Aubrey, D. G., & Friedrichs, C. T. (1991). Nonlinear hydrodynamics in
 883 shallow tidal inlet/bay systems. In *Tidal Hydrodynamics* (pp. 321–339).
- 884 Stewart, R. W. (1989). The no-slip constraint and ocean models. *Atmosphere-Ocean*,
 885 *27*(3), 542–552. doi: 10.1080/07055900.1989.9649351
- 886 Stommel, H. (1948). The westward intensification of wind-driven ocean cur-
 887 rents. *Transactions, American Geophysical Union*, *29*(2), 202. doi:
 888 10.1029/TR029i002p00202
- 889 Tee, K. T. (1976). Tide-induced residual current, a 2-D nonlinear numerical tidal
 890 model. *Journal of Marine Research*, *34*, 603–628.
- 891 Tee, K. T. (1977). Tide-Induced Residual Current—Verification of a Numerical
 892 Model. *Journal of Physical Oceanography*, *7*(3), 396–402. doi: 10.1175/1520
 893 -0485(1977)007<0396:TIRCOA>2.0.CO;2
- 894 Thompson, K. R., Lazier, J. R. N., & Taylor, B. (1986). Wind-forced changes in
 895 Labrador Current transport. *Journal of Geophysical Research*, *91*(C12), 14261.
 896 doi: 10.1029/JC091iC12p14261
- 897 Umlauf, L., & Burchard, H. (2003). A generic length-scale equation for geophysical
 898 turbulence models. *Journal of Marine Research*, *61*(2), 235–265. doi: 10.1357/
 899 002224003322005087
- 900 Umlauf, L., & Burchard, H. (2005). Second-order turbulence closure models for geo-

- 901 physical boundary layers. A review of recent work. *Continental Shelf Research*,
902 25(7-8), 795–827. doi: 10.1016/J.CSR.2004.08.004
- 903 Weatherall, P., Marks, K. M., Jakobsson, M., Schmitt, T., Tani, S., Arndt, J. E., ...
904 Wigley, R. (2015). A new digital bathymetric model of the world's oceans.
905 *Earth and Space Science*, 2(8), 331–345. doi: 10.1002/2015EA000107
- 906 Woodworth, P. L., Hughes, C. W., Bingham, R. J., & Gruber, T. (2012). Towards
907 worldwide height system unification using ocean information. *Journal of*
908 *Geodetic Science*, 2(4), 302–318. doi: 10.2478/v10156-012-0004-8
- 909 Wu, Y., Chaffey, J., Greenberg, D. A., Colbo, K., & Smith, P. C. (2011).
910 Tidally-induced sediment transport patterns in the upper Bay of Fundy:
911 A numerical study. *Continental Shelf Research*, 31(19), 2041–2053. doi:
912 10.1016/j.csr.2011.10.009